

Static and dynamic performance of the RBRargo³ CTD

² M. Dever^{a,b}, B. Owens^b, C. Richards^c, S. Wijffels^b, A. Wong^d, I. Shkvorets^a, M. Halverson^a,
³ G. Johnson^a

^a RBR, Ottawa, Canada

^b Woods Hole Oceanographic Institution, Woods Hole, USA

⁶ ^c Bedford Institute of Oceanography, Department of Fisheries and Oceans Canada, Dartmouth,
⁷ Canada

^d School of Oceanography, University of Washington, Seattle, WA, USA

⁹ Corresponding author: M. Dever, mathieu.dever@rbr-global.com

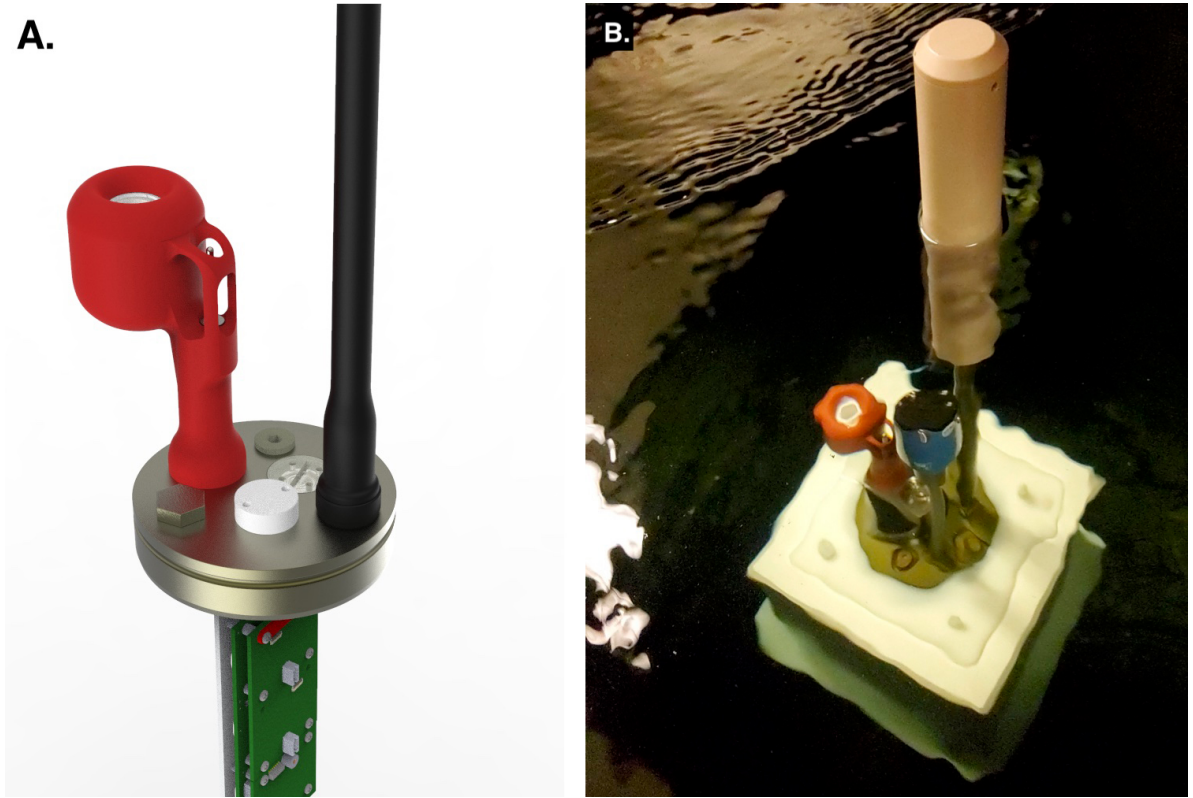
¹⁰ ABSTRACT: The static and dynamic performances of the RBRargo³ are investigated using a
¹¹ combination of lab-based and in situ datasets from floats deployed in an Argo Program pilot
¹² program. Long term deployments show no significant drift in salinity. Static accuracy of salinity
¹³ is significantly improved using (1) a time lag for temperature, (2) a quadratic pressure dependence
¹⁴ and (3) by laboratory calibrating each RBRargo³ for a range of pressures. The presence of two
¹⁵ different adjustment timescales is unravelled: a long-term adjustment O(120 s), driven by the
¹⁶ temperature difference between the interior of the conductivity cell and the water, and a short-term
¹⁷ adjustment O(5-10 s), associated by the initial exchange of heat between the water and the inner
¹⁸ ceramic. Corrections for these effects, including dependence on profiling speed are developed.
¹⁹ The strong speed dependence of the dynamic corrections suggests that profiling at higher speeds
²⁰ (> 15 cm/s) would help minimize dynamic errors.

21 **1. Introduction**

22 Diversification of Conductivity-Temperature-Depth (CTD) instrumentation for the Argo program
23 is crucial to avoid "points of single failure" (Roemmich et al. 2019). As an alternative CTD to the
24 one currently used on Argo floats, the RBR^{argo}³, manufactured by RBR Ltd., was approved for
25 a trial phase to assess its in-situ performance. Several floats equipped with the RBR^{argo}³ have
26 thus been deployed and a task team with members from the Argo community and RBR formed
27 in 2020 to assess instrument accuracy across a range of ocean regimes, help improve calibrations,
28 and develop the procedures to yield the highest data quality.

29 The RBR^{argo}³ conductivity cell relies on a different working principle than the SBE41CP CTD
30 currently used on Argo floats, which relies on an electrode-based measurement of conductivity
31 within a borosilicate glass cell through which water is actively and continuously pumped (Lueck
32 1990). The RBR^{argo}³, on the other hand, uses a free-flushing, low aspect ratio conductivity cell
33 (Figure 1; Halverson et al. 2020b). Conductivity measurements of the seawater in the vicinity of
34 the cell are made according to Faraday's law of induction, using two toroidal coils – a generating
35 coil and a receiving coil. An alternating voltage is applied to the generating coil, producing a
36 time-varying magnetic field and thereby inducing a current in the seawater inside and surrounding
37 the cell (Figure 1). The induced current loops through the seawater and passes through the center
38 of the receiving coil, generating a secondary current. The measured current in the receiving coil is
39 proportional to the conductivity of the seawater.

42 The static accuracy at sea-level of the RBR^{argo}³ is stated to be $\pm 0.003 \text{ mS/cm}$, $\pm 0.002 \text{ }^{\circ}\text{C}$,
43 and $\pm 1 \text{ dbar}$ for conductivity, temperature, and pressure, respectively. However, compressibility
44 effects can affect the static accuracy of conductivity at high pressures, and sensor drift can degrade
45 the static accuracy of conductivity measurements over time. The profiling nature of Argo floats
46 also generate dynamic errors in CTD observations (Lueck and Picklo 1990; Morison et al. 1994;
47 Johnson et al. 2007). In fact, dynamic errors emerge in CTD observations when collected from any
48 moving platform sampling through a temperature gradient, and are proportional to the amplitude
49 of the temperature gradient. These dynamic errors are generated by different processes linked to
50 the physical arrangement of the sensors, the inherent response time of the sensors, and the thermal
51 inertia of the conductivity cell.



40 FIG. 1. (A.) Rendering of an RBRargo³ mounted on an Argo float cap. (B.) Photo of the RBRargo³ mounted
41 on an Argo float during calibration (credits Kai Malorny).

52 In this study, each of these sources of error are characterized and post-processing techniques are
53 developed to correct these errors in order to improve the resulting data accuracy.

54 **2. Theoretical Framework**

55 *a. Static-accuracy and compressibility correction*

56 Static accuracy of the RBRargo³ is determined during the calibration process at RBR, and detailed
57 on the calibration certificate provided with each RBRargo³. Instrument calibration is typically
58 performed at atmospheric pressure. At higher pressure, however, the geometry of the conductivity
59 cell on the RBRargo³ elastically deforms, changing the path of the current in the sampled seawater,
60 and therefore introducing a pressure-dependent bias in the conductivity measurements. This
61 compressibility error is expected to be repeatable from profile to profile and to vary for each CTD
62 (see Section 4).

63 *b. Sensor stability*

64 Each float deployed as part of the Argo program is expected to have a life expectancy of a
65 minimum of 5 years. Sensors onboard floats must therefore demonstrate not only good stability
66 from profile-to-profile, but also over timescales on the order of years. Salinity drift is one of the
67 main challenges the Argo program faces (Wong et al. 2020). Stability of salinity estimates from
68 Argo floats can be affected by many different factors, including biofouling, biocide leakage, or
69 degradation of the cell over time such as deformation or seawater penetration (Wong et al. 2003,
70 2020). Assessing long term stability does require ‘ageing’ the sensor on a float following an Argo
71 mission, during which the CTD is at 1000 dbar for 90% of its lifetime.

72 *c. Dynamic errors and their impact on salinity estimation*

73 Conductivity in the ocean is to first order dominated by temperature, with salinity a relatively mi-
74 nor player. Thus any mismatch between simultaneous temperature and conductivity measurements
75 used to estimate salinity can generate large errors. For a profiling CTD, two types of dynamic
76 errors affect salinity estimates: (1) a time lag between temperature and conductivity measurements
77 and (2) a temperature difference between the fluid at the thermistor and in the measurement volume
78 of the conductivity cell due to its larger thermal inertia (Lueck 1990; Johnson et al. 2007). Both
79 of these dynamic errors can be observed in-situ and are especially obvious when a CTD profiles
80 through a temperature interface into a relatively homogeneous layer, which typically occur in re-
81 gions of double-diffusive instability or near the base of the surface mixed layer. Figure 2 shows an
82 example profile collected by an RBRargo³ -equipped ALAMO float in the Caribbean Sea, where
83 both the salinity and the potential density anomaly clearly exhibit artificial features at temperature
84 interfaces (Jayne and Bogue 2017; Sanabia and Jayne 2020). The error in salinity (and potential
85 density) has both a short time scale, O(5-10 sec), seen as a high salinity/density spike near the
86 lower boundary of the well-mixed layer, and a longer time scale O(120 seconds) that extends over
87 much of the mixed-layers and is best visible as an artificial negative slope in the potential density
88 as a function of pressure.

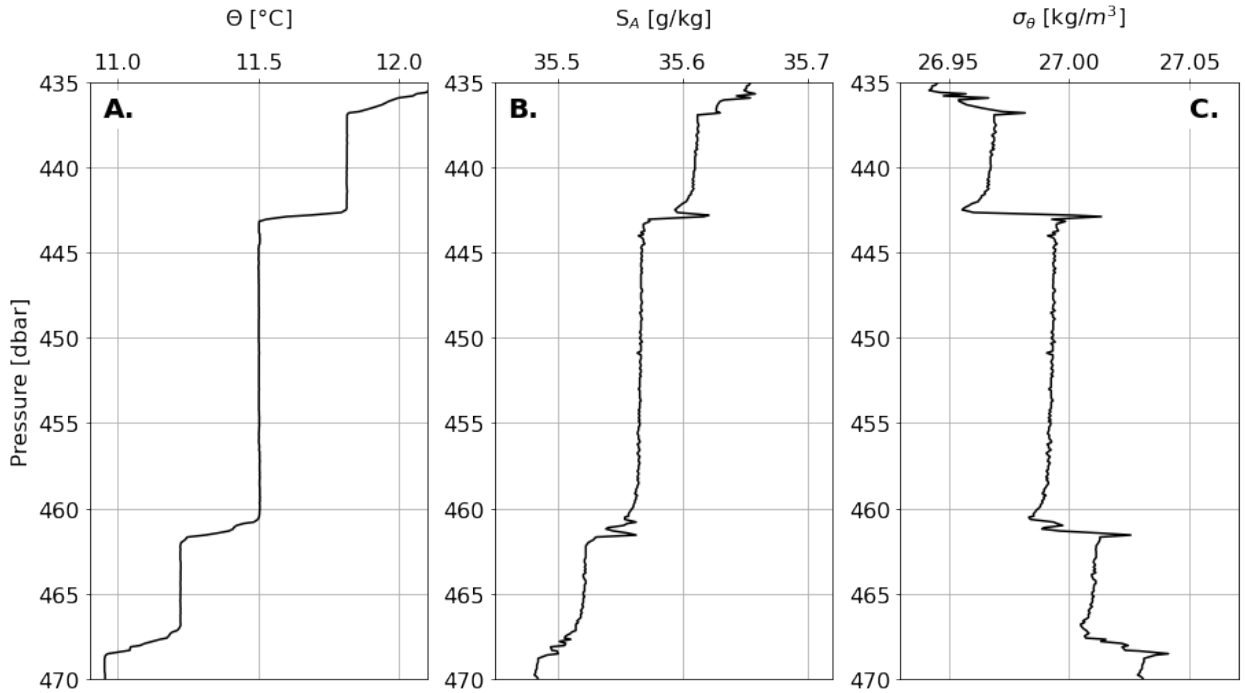


FIG. 2. Example profile from ALAMO float 9139 in the Caribbean Sea (profile 52), showing (A.) the conservative temperature, (B.) the absolute salinity, and (C.) the potential density anomaly. The staircase structure of the water column highlights dynamic errors in both salinity and density at sharp interfaces, where both spiking and thermal inertia errors can be seen. Data Courtesy of Drs Sanabia (US Naval Academy) and Jayne (Woods Hole Oceanographic Institution).

1) RESPONSE TIME AND SENSOR MISALIGNMENTS

Misalignments between temperature and conductivity measurements generate errors in salinity estimates, often called "salinity spiking" (Horne and Toole 1980; Ullman and Hebert 2014; Dever et al. 2020). This misalignment is referred to as a "C-T lag", and is generated by two separate mechanisms:

1. The physical separation between the thermistor and the conductivity cell. As it takes time for the sampled water parcel to travel from the thermistor to the volume sampled by the conductivity cell, this "advection lag" is directly proportional to the distance between the thermistor and the conductivity cell, and is therefore dependent on the flow speed through the CTD. The RBRargo³ CTD has been designed to minimize the spatial separation between conductivity and temperature, and thus the advective C-T lag (see Figure 1).

105 2. The inherent response time of the thermistor. The thermistor responds more slowly to a
106 change in temperature than the conductivity cell who is virtually instantaneous due to the
107 fact that it is an electrical measurement and does not rely on diffusion processes the way the
108 thermistor does. This difference in response time introduces an apparent time-lag between
109 the temperature and conductivity, resulting in spiking in the computed salinity (Horne and
110 Toole 1980). This C-T lag is caused by the inherent properties of the thermistor and can be
111 considered to be independent of flow-speed to the first degree of approximation.

112 This error can be seen in Figure 2, with some evident salinity spiking coinciding with sharp
113 temperature gradients, and can be corrected by shifting the measured temperature in time using:

$$T_{cor}(t) = T_{meas}(t + \Delta t) \quad (1)$$

114 where T_{cor} is the lagged temperature, T_{meas} is the raw temperature, and Δt is the prescribed lag.
115 Other approaches than a simple time-lag are sometimes considered to correct for the C-T lag, such
116 as sharpening algorithms (Fozdar et al. 1985; Bittig et al. 2014; Johnson et al. 2007). Sharpening
117 algorithms present the advantage to further reduce the salinity spiking by reconstructing fine-scale
118 gradients that are not captured by the sensor. However, the reliability of all these techniques
119 depends on both the amplitude and phase reconstruction. The time-lag approach was deemed to be
120 a good compromise between phase and amplitude reconstruction of the signal across the frequency
121 range.

122 2) THERMAL INERTIA ERRORS

123 As the CTD travels through a temperature gradient, heat is exchanged between the conductivity
124 cell and a thin boundary layer attached to the cell, which changes the temperature averaged over
125 the conductivity measurement volume from that measured by the thermistor. Thus, the calculated
126 salinity must use a temperature adjusted for the heat flux into the measurement volume. This is
127 a well-known, but poorly constrained, error in CTD measurements generally, and is the focus of
128 a research effort that has been ongoing for over three decades (Lueck and Picklo 1990; Morison
129 et al. 1994; Johnson et al. 2007; Martini et al. 2019; Johnson 2020; Halverson et al. 2020b). As
130 described by Lueck (1990), the heat flux at the cell boundary will depend on the profiling speed and
131 the difference between the cell surface temperature and T_{cor} while the thickness of the boundary

layer which determines the contribution to the measurement averaged temperature will depend on the profiling speed. The surface temperature of cell will depend on the heat conduction within the cell.

While the transfer of heat into the fluid depends on the skin temperature of the cell, the change in the skin temperature will depend on the thermal conductance of the cell components. As shown in Figure 1, the cell is constructed from materials for which the thermal conductance varies by more than a factor of 20.

In a cylindrical coordinate system, the equation describing the diffusion of heat can be written as:

$$\rho C_p \frac{\partial T}{\partial t} = \frac{1}{r} \frac{\partial}{\partial r} \left(r \lambda \frac{\partial T}{\partial r} \right) \quad (2)$$

where ρ is the density of the material, C_p is the heat capacity, T is the temperature inside the conductivity cell, r is the distance from the center of the ceramic annulus (see Figure 1), and λ is the thermal conductivity.

After a short time the heat content of material near the cell boundary changes slowly, so that the left hand side of Equation 2 approaches zero. Thus for longer timescales the heat conductance into the cell can be approximated using the average thermal conductance and the difference between the temperature measured inside the cell which must equal the heat flux through the surface boundary layer. This approximate balance leads to an expression for the temperature anomaly at long time scales:

$$T_{long} = \text{ctcoeff} (V_p) \times (T_{cond} - T_{cor}) \quad (3)$$

where T_{long} is the temperature anomaly in the sampled volume due to long-term thermal inertia, T_{cond} is the internal temperature of the conductivity cell, T_{cor} is the lagged temperature of the seawater, and ctcoeff is a scaling coefficient that is a function of the profiling speed V_p . The profiling speed is defined as the velocity of the water at the CTD.

On shorter timescales, the approach used to correct for thermal inertia errors has traditionally relied on an idealized model developed by Lueck (1990) and slightly modified by Lueck and Picklo (1990) and Morison et al. (1994). The model, hereafter referred to as L&P90, is essentially a

157 recursive filter that aims to estimate the short-term temperature anomaly of the volume of water
158 present in the conductivity cell as the CTD travels through a seawater temperature gradient. It
159 relies on two key parameters, namely α and τ , that drive the amplitude and timescale of the filter.
160 It is expressed in discrete form using the following equation (Morison et al. 1994):

$$T_{short}(n) = -bT_{short}(n-1) + a(T_{cor}(n) - T_{cor}(n-1)) \quad (4)$$

161 where T_{short} is the short-term temperature anomaly estimated by the filter, and n is the index for a
162 discrete measurement. The two coefficients a and b are computed using:

$$\begin{aligned} a &= \frac{4f_N\alpha\tau}{1+4f_N\tau} \\ b &= 1 - \frac{2a}{\alpha} \end{aligned} \quad (5)$$

163 where f_N is the Nyquist frequency, and α and τ are empirically determined parameters (see section
164 4).

165 The total estimated temperature of the sampled volume can be estimated by combining both of
166 those temperature anomalies with the measured temperature:

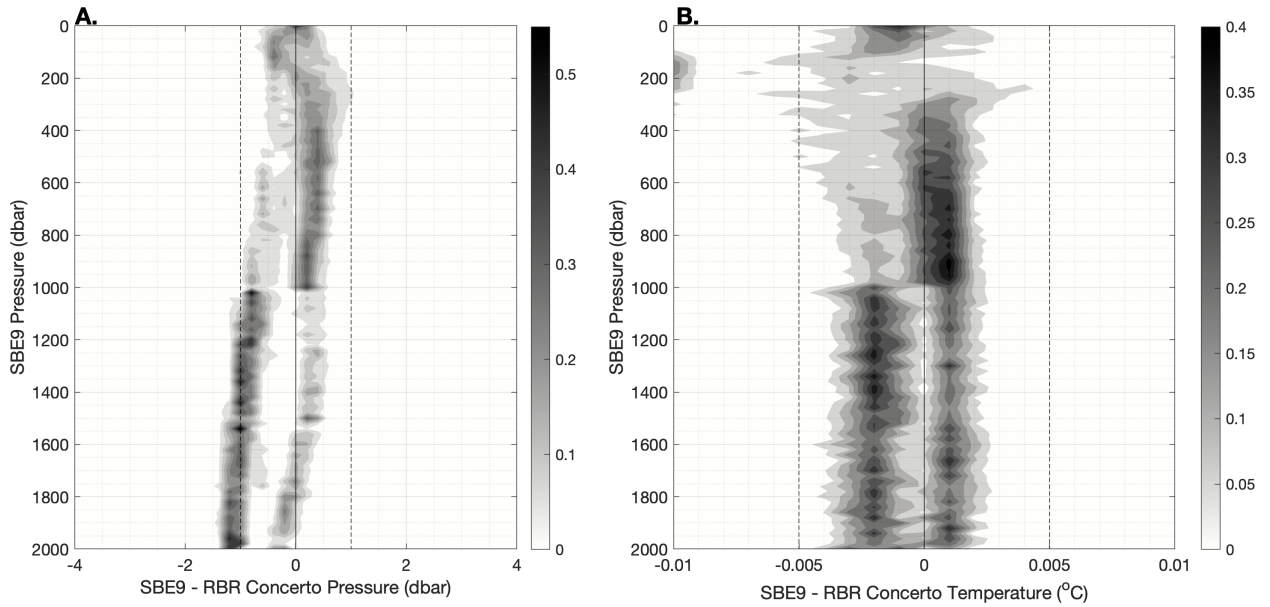
$$T_{cell} = T_{cor} + T_{anomaly} = T_{cor} + T_{long} - T_{short} \quad (6)$$

167 where T_{cell} is the estimated temperature of the sampled volume, corrected for both long- and
168 short-term thermal inertia, and is used to derive the corrected salinity.

169 3. Datasets and Methodology

170 a. Static accuracy and compressibility correction

171 The static accuracy of temperature and pressure were assessed utilizing data from four ship-board
172 campaigns (Table A1), where RBRconcerto³ CTDs, which use equivalent thermistors and pressure
173 sensors as the RBRargo³, were mounted on CTD rosettes equipped with SBE9 CTDs. The latter



187 FIG. 3. (A.) Pressure differences between SBE9 and the RBR³ 's analogous RBR*concerto*³, across all
 188 voyages and sensor pairs, after synchronisation (see Section a). Plotted is the frequency distribution in each 20
 189 dbar SBE9 pressure bin, expressed as a fraction of the total pairs in 0.2 dbar increments of the difference. (B.)
 190 Same as (A.) for temperature. Plotted is the frequency distribution in each 20 dbar SBE9 pressure bin, expressed
 191 as a fraction of the total pairs in 0.001 °C increments of the difference.

194 typically had two pairs of SBE4 temperature sensors and pressure was measured by a Para-scientific
 195 quartz sensor. The SBE9 is powered via a cable to the ship and reports back 24 Hz data. The
 196 accuracy of the SBE9 system post calibration is 0.001 °C and 0.015% range for pressure (0.3 dbar).
 197 The RBR CTDs on the rosettes were internally recording and were typically set to sample at 8 to
 198 12 Hz. A first gross comparison was made of the two SBE9 channels, and the primary was chosen
 199 for the temperature comparison below.

200 To compare pressure readings, the SBE9 and RBR data streams were interpolated to the RBR's
 201 timebase, and then the cross-correlations function was computed for pressure. The computed
 202 lags maximizing the cross-correlation function were then used to synchronize the data streams,
 203 exploiting the small (1-2dbar) pressure changes associated with surface wave action on the CTD
 204 fall and rise rates. Once synchronized, the difference of the pressures was found, and then binned
 205 every 20 dbar (using the SBE9 pressure) across all 4 voyages and all RBR CTDs (Table A1). In
 206 each 20 dbar bin, the distribution of pressure differences was calculated (Figure 3).

192 A similar direct approach to examining temperature differences is precluded by the varying effect
193 of water flow past the sensors within each rosette (the sensors are mounted at different heights above
194 deck), and wake effects, which introduces both bias and noise to the comparison. To reduce these
195 effects, we again use lagged correlations of the high-resolution temperature data streams from each
196 sensor. For each cast and SBE9/RBR sensor pair, we perform a lagged correction of temperature
197 tendency in each 15 dbar bin. For bins where the temperature tendency correlation coefficient is
198 > 0.5, we apply the lag, typically between 0-1 second) to align the temperature traces and then
199 find the temperature differences. Thus for bins where wake effects de-correlate the temperature
200 variance, the data are not used. As for pressure, the temperature differences are binned to produce
201 frequency distributions in 20 dbar pressure bins (Figure 3).

202 Laboratory measurements are preferable to in-situ data for characterizing compressibility effects
203 on the conductivity sensor. For example, the natural variability in the upper layer of the ocean
204 is larger than the target accuracy of the conductivity sensor (± 0.003 mS/cm). In a laboratory
205 pressure tank data is collected for a range of pressures up to the maximum pressure rating (i.e.,
206 2,000 dbar) of the RBRargo³. The temperature of the pressure tank is maintained between 1 and
207 2 °C to represent ocean conditions at depth. The salinity in the pressure tank is determined from
208 water samples before and after the pressure cycling using a Guildline 8400B Autosal.

209 The effects of compressibility on the conductivity measurement can be modeled using a cubic
210 adjustment of the form:

$$C_{meas} = \frac{C_{raw}}{1 + X2 \cdot P + X3 \cdot P^2 + X4 \cdot P^3} \quad (7)$$

211 where C_{raw} is the raw conductivity measured by the instrument, P is the sea pressure, ($X2$, $X3$,
212 $X4$) is the set of compressibility correction coefficients, and C_{meas} is the compressibility-corrected
213 conductivity.

214 in-situ data from the YMC cruise in 2019 was used to validate the compressibility correction
215 developed for two specific RBRargo³ CTDs (see Table A1). A direct comparison can thus be
216 made between the compressibility-corrected salinity collected from the RBRargo³ CTDs and the
217 shipboard CTD, both cross-calibrated with water samples (see Appendix 5).

218 *b. Sensor stability*

219 A robust delayed-mode analysis method has been developed to identify salinity sensor drift in
220 Argo profiling floats (Owens and Wong 2009; Cabanes et al. 2016). Nezlin et al. (2020) used this
221 method to characterize the long-term stability of the RBRargo³ on six early-deployed Argo floats.
222 Here, we provide an update on the stability of the current RBRargo³ fleet, using nineteen RBRargo³
223 floats that have been sampling in the ocean for over six months. The time series of salinity from
224 these nineteen RBRargo³ CTDs are compared against objectively mapped salinity from a CTD
225 reference database. Comparisons are done on isotherms selected from the least variable part of the
226 T-S curve in order to minimize the effects of natural variability in the comparison.

227 *c. Dynamic behavior of conductivity measurements*

228 1) RESPONSE TIME AND SENSOR MISALIGNMENTS

229 To align temperature and conductivity measurements collected by the RBRargo³, an optimal
230 temporal lag is determined to correct the temperature observations. The optimal C-T lag, which
231 combines the two mechanisms detailed in Section 2, is determined by maximizing the cross-
232 correlation between the first-order differences in conductivity and in temperature (Barth et al.
233 1996; Ullman and Hebert 2014; Dever et al. 2020). This approach relies on the assumption that
234 changes in conductivity over short spatial scales are mostly driven by changes in temperature.
235 The analysis is applied to data collected by six different RBRargo³ units deployed over different
236 cruises (see Table A1). Only downcasts sampling deeper than the mixed layer depth are used, as
237 the RBRargo³ were pointing downwards in all deployments. The resulting dataset comprises a
238 total of 380 profiles. Each considered profile is separated into 7 s segments. For each segment, the
239 cross-covariance between the first-order differences in temperature and in conductivity is computed
240 for a series of lags. The lag maximizing the cross-covariance is recorded if the cross-covariance
241 is greater than 0.5. Otherwise, the segment is rejected from the analysis, as it likely violates
242 the fundamental assumption of this method. Segments located above the mixed layer depth are
243 also ignored, as they would skew the results towards a maximum cross-covariance at a zero lag.
244 A second-order polynomial is fit to the cross-covariance function using three consecutive points
245 centred on the lag maximizing the cross-covariance. The polynomial's maximum determines the
246 "optimal lag" for the segment. Fitting a polynomial allows for non-integer lags, which is key to

247 further remove dependence on the sampling rate. Finally, the optimal lags determined from all
248 eligible segments are concatenated into a Probability Distribution Function (PDF) as a function
249 of the profiling speed averaged over the length of the segment. A total of 25,488 segments are
250 considered to determine the C-T lag for the thermistor on the RBRargo³. A Gaussian distribution
251 is fit to the PDF in each profiling rate bin to extract the mean value of the C-T lag to be used to
252 align temperature and conductivity readings.

253 2) THERMAL INERTIA ERRORS

254 An idealized experimental setup was designed in the laboratory to characterize how the RBRargo³
255 conductivity cell responds to thermal gradients. An RBRargo³ CTD was transferred from a cold
256 bath ($T \approx 6^\circ\text{C}$) into a large recirculating flume in thermal equilibrium with the room temperature
257 ($T \approx 19^\circ\text{C}$, $S \approx 30$) to simulate a temperature step change in saltwater. The flume consists of a channel
258 50 cm wide by 50 cm high, and about 8 m long. At the upstream end of the channel, a collimator is
259 used to smooth out the turbulence in the flow entering the channel. At the downstream end of the
260 channel, a propeller forces water through the recirculating loop at a constant speed, which can be
261 adjusted by changing the rotational speed of the propeller. The water speed is monitored upstream
262 of the RBRargo³ CTD by a current meter (Nortek Vector) with its sample volume centred on the
263 same depth as the RBRargo³ CTD. Six different water speeds were configured between 7 and 45
264 cm/s, with two separate plunges at each speed.

265 A correction for the long-term adjustment of the conductivity cell is computed using Equation 3.
266 The coefficient `ctcoeff` is determined by doing a linear fit of the temperature anomaly as a function of
267 the temperature difference between the interior of the conductivity cell and the water surrounding
268 the cell. For each plunge, data collected in the first 90 s are ignored to avoid contamination
269 from the short-term thermal inertia adjustment. The temperature anomaly is then binned to avoid
270 overweighting the fit towards low temperature gradients across the conductivity cell.

271 The short-term error of the RBRargo³ conductivity cell responds to thermal gradients with a
272 timescale on the order of seconds, and cannot be addressed using the same approach as for its
273 long-term counterpart, mostly for practical reasons. The physical processes driving this short-term
274 adjustment are hypothesized to be related to the exchange of heat between the water located within
275 the cell's channel, and the ceramic itself. It is operationally challenging to directly measure the

temperature of the ceramic. L&P90 is used to correct the short-term thermal inertia on conductivity (see Equation 4). The timescale of the short-term thermal inertia adjustment is estimated first, using a similar approach to Lueck and Picklo (1990): The slope of the logarithm of the normalized salinity time series is computed over the first 15 s after the temperature change to determine the e-folding timescale τ , where $t = 0$ is defined as the time where the marine temperature reaches 99% of its final value. The optimal value of α is then computed by minimizing the root-mean-squared-error (RMSE) in the salinity residuals (Figure 10), referenced to the final static salinity.

The results obtained from the flume are validated using in-situ datasets collected from two different profiling floats (see Table A2). These specific floats were selected for several reasons: First, it is important that the data resolution is high enough to capture the relevant timescales. In fact, most profiling floats transmit data that are binned into pressure bins, thus smoothing out the relevant timescales and making the thermal inertia corrections inefficient, especially over the shorter timescales. Second, it is necessary to have well-defined, sharp, interfaces followed by a well-mixed layer to be able to visualize the salinity adjustment due to thermal inertia. This is often the case in either thermohaline staircases, or at the base of the surface mixed layer. Finally, these floats were selected because they span different ocean basins (Caribbean Sea and sub-arctic North-Atlantic), and a range of profiling speeds ranging from 3 cm/s to 20 cm/s.

4. Results

a. Static accuracy and compressibility correction

1) PRESSURE AND TEMPERATURE ACCURACY

Figure 3 demonstrates the static accuracy of both pressure and temperature on the RBRargo³ when compared to a SBE9 on a CTD rosette. The full data set reveals that the instruments agree to within 1.5 dbar across all pressure ranges. For temperature, we find that the vast majority of paired readings give temperature differences less than 0.003°C, which is within the specifications of the SBE9 and RBRargo³ CTDs, confirming the stated accuracy for temperature on the RBRargo³ across the pressure ranges examined.

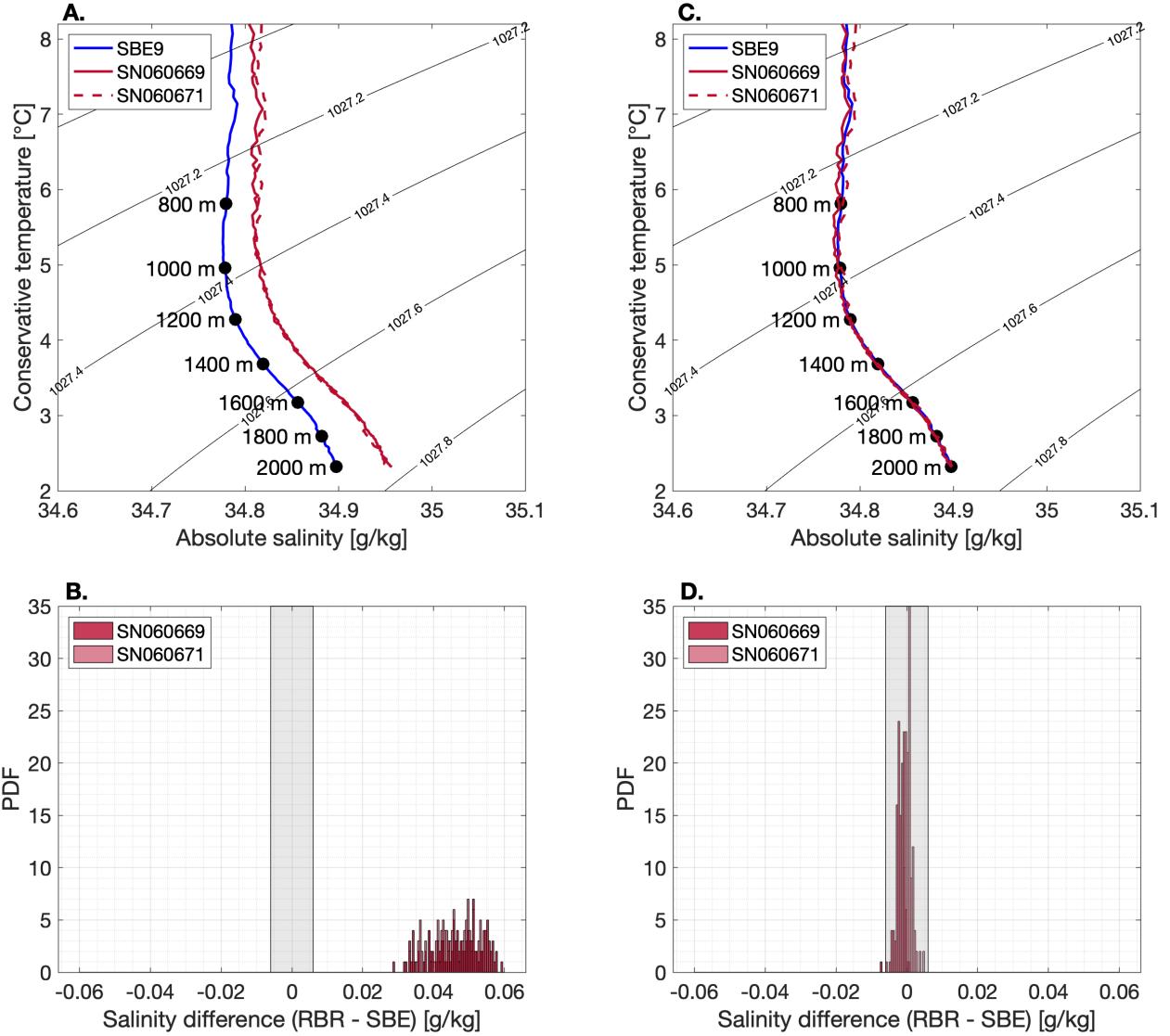
302 2) CONDUCTIVITY STATIC ACCURACY

303 The amplitude of the compressibility error was characterized by directly comparing the salinity
304 profiles obtained from an SBE9 and RBRargo³ CTDs on a variety of cruises. Comparing the two
305 salinity records in the deeper part of the water column (e.g., >800 dbar), where the water masses
306 tend to be more stable, revealed that the salinity difference between the RBRargo³ CTDs and the
307 shipboard cross-calibrated SBE9 has a depth-dependent bias. An example of this bias is showed
308 in Figure 4 using the data from the YMC cruise (see Table A1). Both RBRargo³ CTDs tested on
309 the YMC cruise have a salty bias that increases with depth, suggesting that the error in salinity is
310 caused by the compressibility of the conductivity cell.

316 The two RBRargo³ CTDs deployed on the YMC cruise were subsequently tested for pressure
317 response in the laboratory, using the setup described in Section a. Customized coefficients were
318 derived for each RBRargo³ CTD, reducing the compressibility-induced salinity error from O(0.02)
319 to <0.003 (Figure 5). The field-based comparison confirms the validity of the newly-derived
320 compressibility correction coefficients from the laboratory: after updating the coefficients in
321 Equation 7, both RBRargo³ CTD compare well to the calibrated SBE9 data, with residuals
322 contained within the combined accuracies of the RBRargo³ and the SBE9 CTDs (Figure 4). Not
323 only the mean of the PDF is brought closer to 0, its standard deviation is also reduced, suggesting
324 that the salinity bias is less dependent on depth. These results indicate that customized parameters
325 for compressibility correction to conductivity can reliably be determined for individual RBRargo³
326 CTDs in the laboratory during the calibration process.

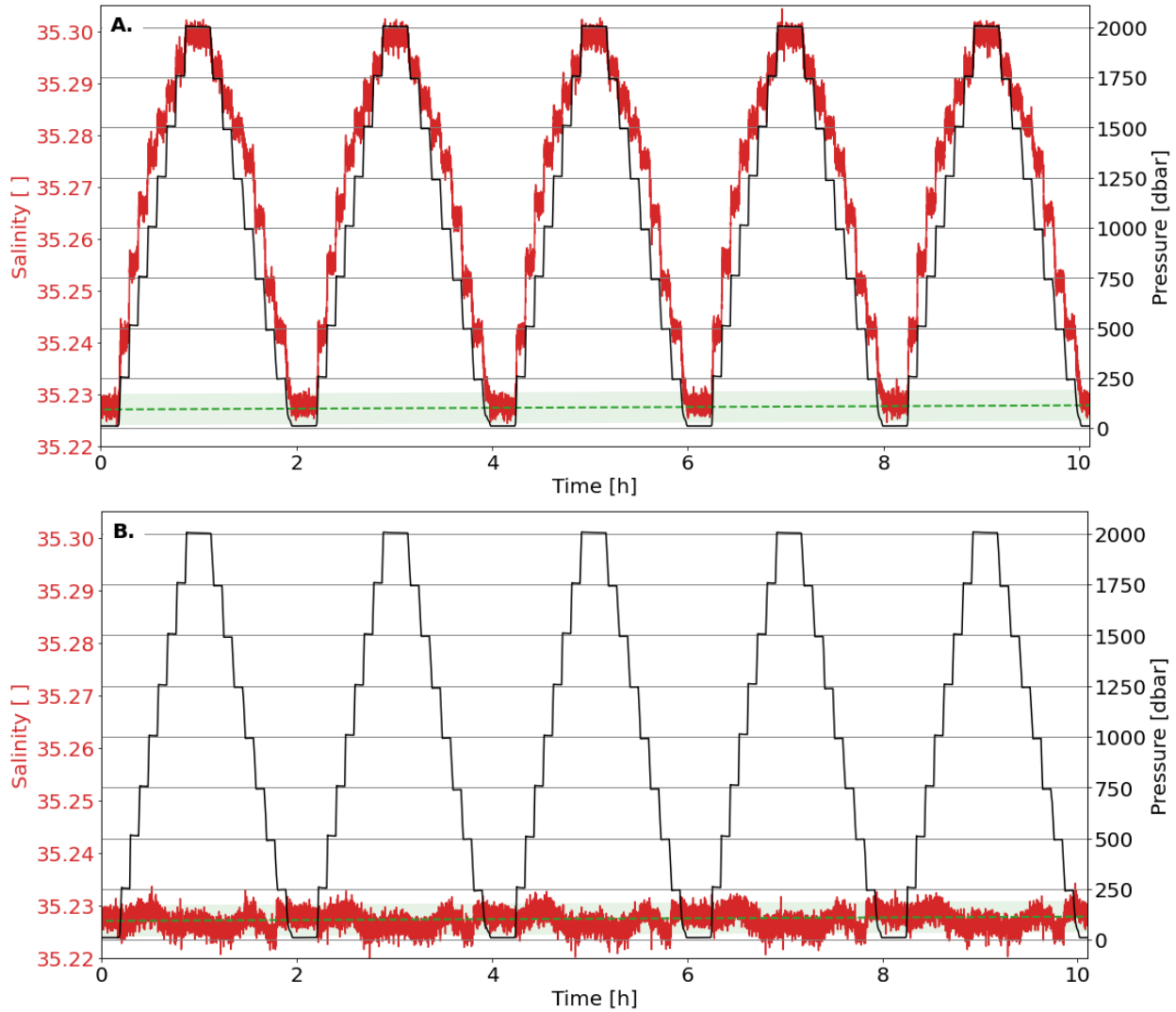
331 *b. Sensor stability*

332 Since the average length of the time series from the nineteen considered RBRargo³ CTDs was
333 only 1.5 years, it is somewhat premature to draw any definite conclusions about the long-term
334 stability of the RBRargo³ CTDs. Nonetheless, salinity measurements from eighteen RBRargo³
335 CTDs showed no sign of sensor drift at the time of analysis, suggesting good sensor stability (Figure
336 6). Only one RBRargo³ suffered from significant drifting (WMO5906299), which was identified
337 to be associated with a malfunction of the float's buoyancy pump. The float was found to have
338 extended surfacing times, sometimes over 24 hours, that correlated with sudden and large fresh
339 salinity errors, suggesting the cell suffered from biofouling due to the abnormally long surfacing



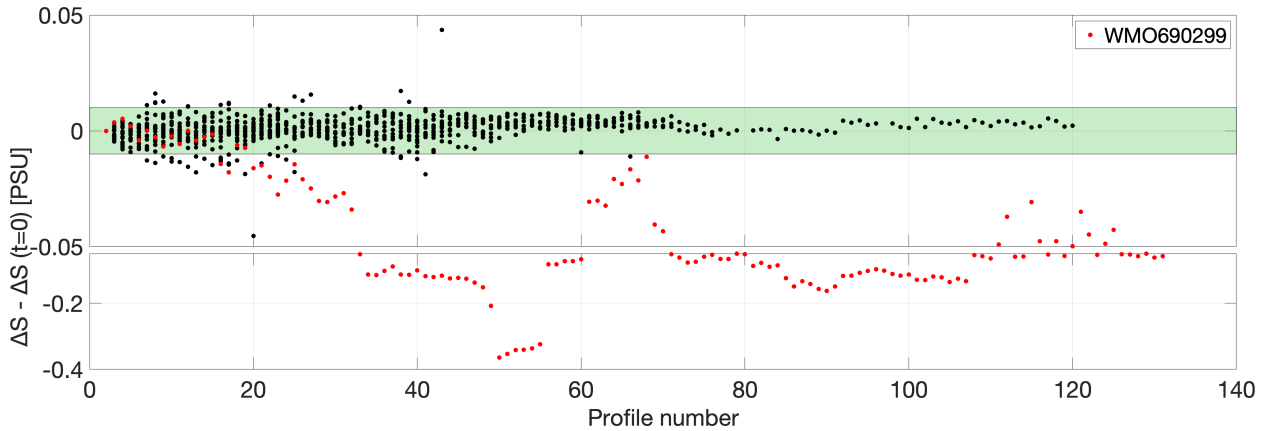
311 FIG. 4. T-S plots of data collected by two RBRargo³ and a SBE9 during the YMC cruise (station 4; Rees, C.
 312 and McMahon, M. 2019) (A.) before and (C.) after applying a customized pressure correction to conductivity.
 313 The corresponding Probability Distribution Functions (PDFs) of the salinity bias for data collected below 800 m
 314 are shown in (B.) and (D.). All three CTDs were cross-calibrated using bottle samples taken on this profile (see
 315 Section 2 and Appendix 5).

340 time (RBR Report 2021). For the remaining eighteen RBRargo³ CTDs, totalling 857 profiles to
 341 date, 94% of profiles have a salinity anomaly smaller than ± 0.01 , falling within Argo's expectation.
 342 As in Section 2, an offset from reference was present for most of the analyzed CTDs, which is



327 Fig. 5. Time series of practical salinity (red line) during pressure cycling (black line). (A.) before pressure
 328 correction is applied, and (B.) after the cubic pressure correction has been applied for the RBR^{Argo³} CTD
 329 SN060671. The reference salinity is super-imposed (dashed green line), with its associated uncertainties (green
 330 shading).

343 due to the sub-optimal compressibility coefficients used on these RBR^{Argo³} CTDs, as previously
 344 discussed.



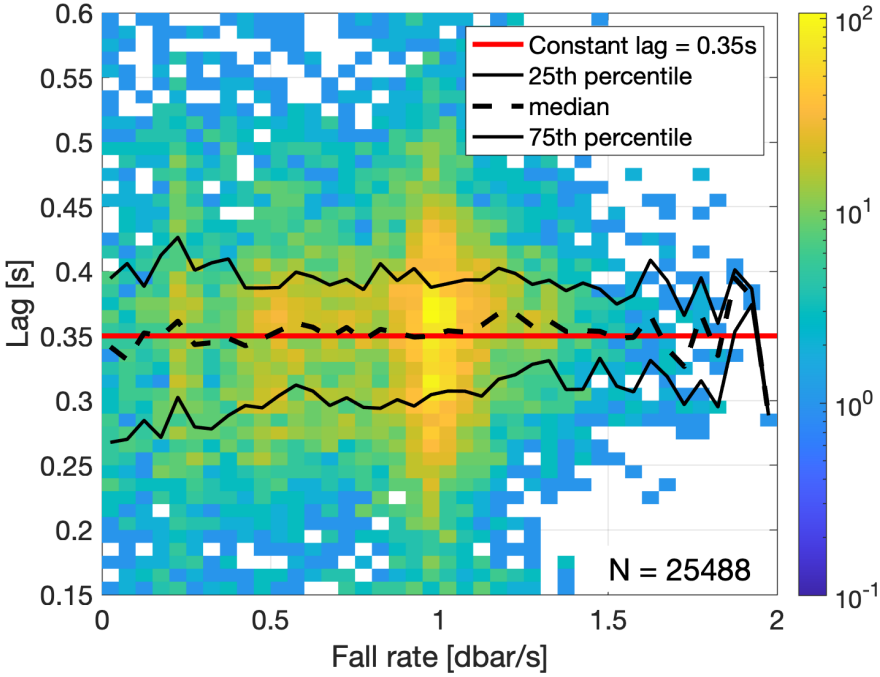
345 FIG. 6. Time series of the salinity bias determined from objectively mapped reference data (Owens and Wong
 346 2009) with respect to the first full-depth profile, for nineteen RBRargo³ CTDs. The green shading indicates +/-
 347 0.01 . Float with WMO5906299 is highlighted in red, as it was identified to drift due to a float malfunction (see
 348 Section 4). Note the break and change in scale in the y-axis.

349 *c. Dynamic behavior of conductivity measurements*

350 1) RESPONSE TIME AND SENSOR MISALIGNMENTS

351 The misalignment between temperature and conductivity measurements (i.e., C-T lag) introduced
 352 by the slower time-response of the thermistor is characterized by applying the analysis detailed
 353 in Section 3. The distribution of “optimal” C-T lags derived from the dataset is shown in Figure
 354 7. Several key points can be extracted from Figure 7: First, the spread between the 25th and 75th
 355 percentiles with respect to the median value is comparable across fall-rates, suggesting that the
 356 distribution of optimal lags can be approximated by a normal distribution. Second, the median
 357 value computed for each individual fall-rate bin is fairly constant and thus does not seem to be a
 358 function of the fall-rate, over the range of rates explored. Third, a constant optimal lag of 0.350 s
 359 ($\sigma = 0.003$ s) can be used for fall-rates slower than 1.5 dbar/s.

360 To validate this empirically-derived C-T lag with an independent dataset, an RBRargo³ CTD is
 361 used in the laboratory to profile downward through a sharp temperature gradient (Figure 8; Schmitt
 362 et al. 2005). It is clear in Figure 8 that the time-response of the temperature lags the response of
 363 the conductivity measurements: Not only the interface is smoother in the temperature signal than
 364 it is in the conductivity measurements, it is also shifted in time (and thus pressure). The computed

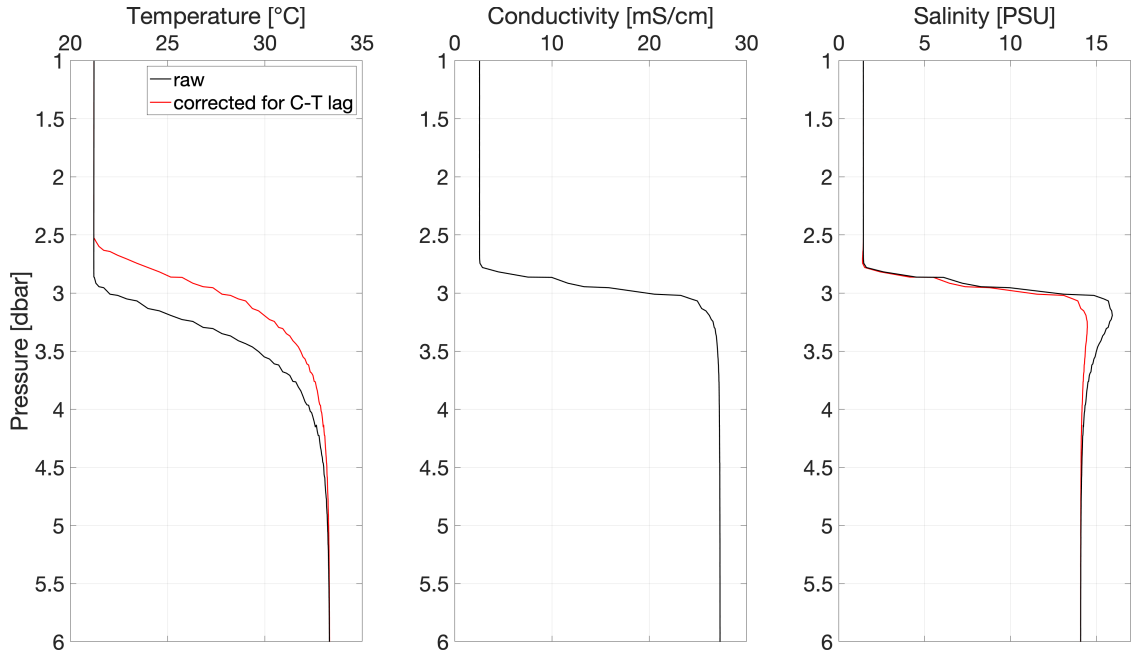


360 FIG. 7. Two-dimensional PDF of the “optimal” C-T lag derived for 25,488 segments, as a function of fall-rate
 361 (see Section 3). Note the logarithmic color scale.

367 salinity exhibits a spike just after the RBR^{argo}³ CTD crossed the interface, with a maximum error
 368 of 1.5 . Once the C-T lag correction is applied, the interfaces in both temperature and conductivity
 369 are centred around ~ 3 dbar. Spiking observed in the raw salinity is now much reduced and the
 370 bottom layer is more homogeneous.

374 2) THERMAL INERTIA ERRORS

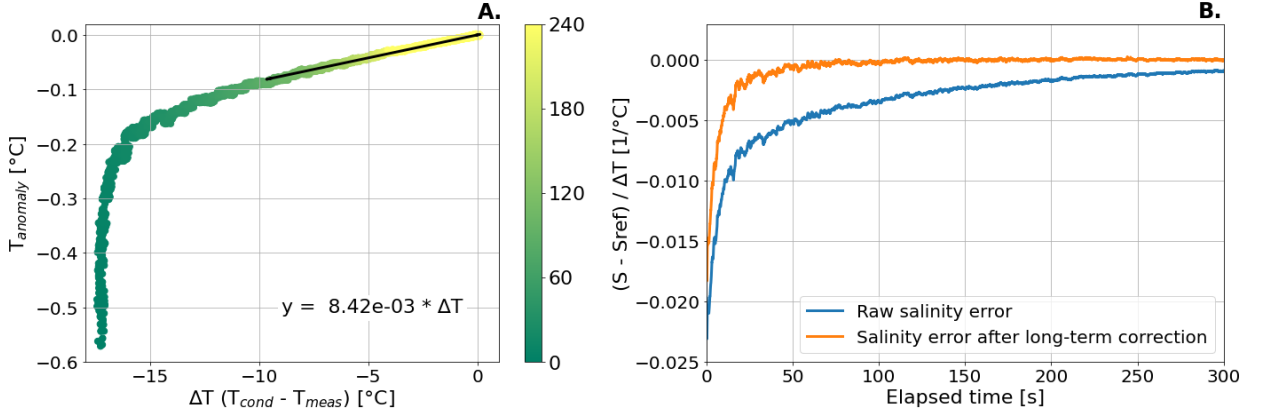
375 Figure 9 shows the two dominant timescales of the thermal inertia adjustment of the salinity after
 376 experiencing a temperature change, and highlights the change in physical processes responsible for
 377 those two different timescales. At first, the salinity error normalized by the temperature change,
 378 is as large as 0.02 1/°C and rapidly adjusts with a characteristic timescale on the order of tens of
 379 seconds. During this first phase, the temperature difference between the water and the internal cell
 380 temperature does not constitute a good predictor, suggesting that the driving mechanism is the heat
 381 exchange between the ceramic and the sampled water volume, as hypothesized in Section 3. For
 382 longer timescales (>30 s), the temperature gradient across the conductivity cell ΔT becomes a good
 383 predictor of the thermal inertia temperature anomaly. As ΔT decreases and the conductivity cell



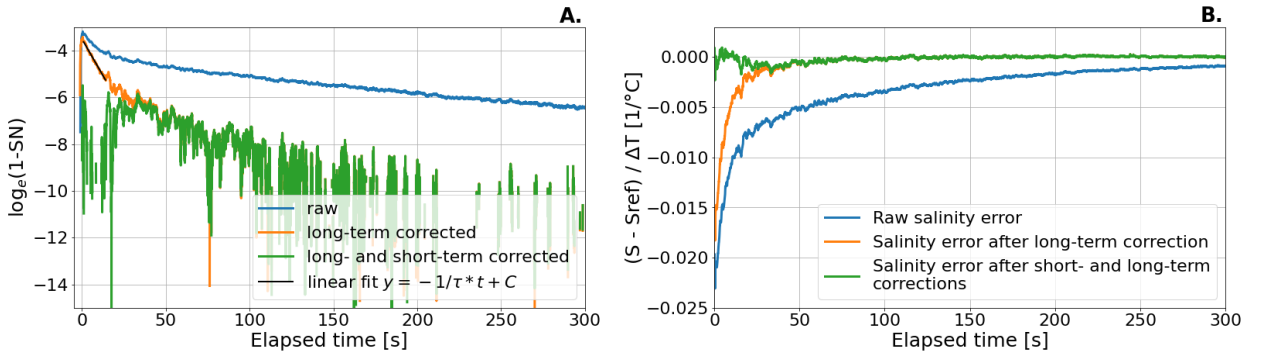
371 FIG. 8. Profiles of temperature, conductivity, and salinity obtained using an RBRargo³ across a sharp
 372 temperature and conductivity interface in a water tank (Schmitt et al. 2005). Lagging the temperature signal in
 373 time by -0.35 s reduces salinity spiking seen at the interface.

384 reaches thermal equilibrium with its surrounding water, the corresponding temperature anomaly
 385 decreases linearly with a constant slope. Once the long-term correction is applied using Equation
 386 3, the transient salinity error depicted in Figure 9 is greatly reduced. The remaining thermal inertia
 387 error is now mostly constrained to the first tens of seconds after the temperature step. For example,
 388 at $V_p = 13.2 \text{ cm/s}$, the salinity error after 60 s drops from 5×10^{-3} to $5 \times 10^{-4} \text{ 1/}^{\circ}\text{C}$.

395 The remaining error in the salinity is attributed to the thermal inertia adjustment over short
 396 timescales. This adjustment over shorter timescales can be seen in the time series of the normalized
 397 salinity in Figure 10, where the logarithm of the normalized salinity decreases linearly with time.
 398 A linear fit over the first 15 s after the temperature step yields an estimate of the e-folding timescale
 399 τ . For example, at $V_p = 13.2 \text{ cm/s}$, the normalized salinity decreases with a time constant of $\tau =$
 400 8.0 s . Using this decaying timescale, it is found that $\alpha = 0.03$ minimizes the RMSE of the salinity
 401 residuals. Figure 10 shows the time series of salinity residuals after correcting for both the long-
 402 and short-term thermal inertia errors for $V_p = 13.2 \text{ cm/s}$, with a maximum salinity residual on the
 403 order of $1 \times 10^{-3} \text{ 1/}^{\circ}\text{C}$.

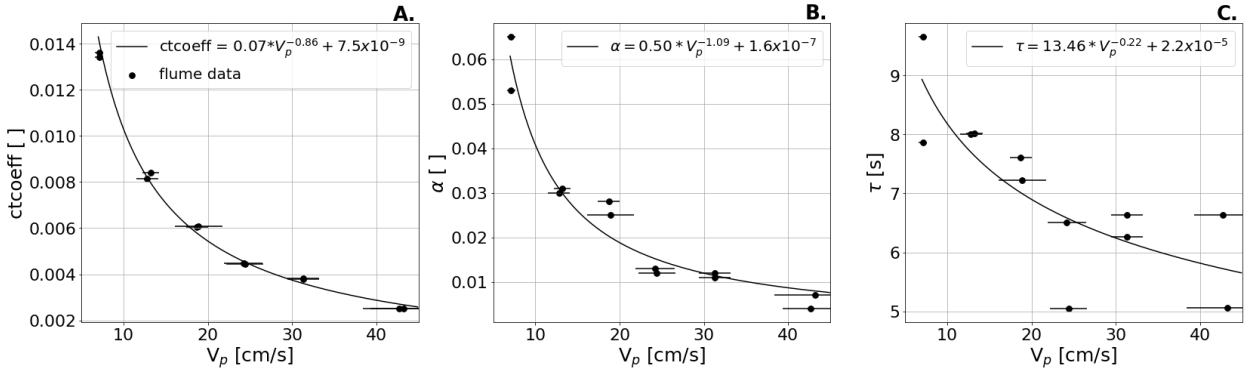


389 FIG. 9. Example of long-term correction for SN208077 at a flow speed of 13.2 cm/s. (A.) Computed
 390 temperature anomaly $T_{anomaly}$ as a function of the temperature difference between T_{cond} and T_{meas} (see Section
 391 a). Colormap shows the time elapsed since the temperature step-change in seconds, and the solid black line
 392 shows the least-squares fit used to compute ctcoeff. (B.) Time series of salinity error during the plunging test,
 393 normalized to the temperature gradient (see Section 2). Raw salinity (blue) is shown along with the corrected
 394 salinity (orange) using Equation 3 and ctcoeff = 8.42×10^{-3} .



404 FIG. 10. Example of short-term correction for SN208077 at a flow speed of 13.2 cm/s. (A.) Time series of the
 405 normalized salinity error. The linear fit used to derive the timescale τ (see Section 2 and Equation 5) is shown as
 406 the solid black line. (B.) Time Series of the salinity error during the plunging test normalized to the temperature
 407 gradient, similarly to Figure 9.

408 All three coefficients used in correcting for thermal inertia errors are expected to vary with the
 409 profiling speed V_p , as the profiling speed affects the thickness of the boundary layer around the
 410 conductivity cell, in turn changing the magnitude and timescale of the heat fluxes(Lueck 1990;



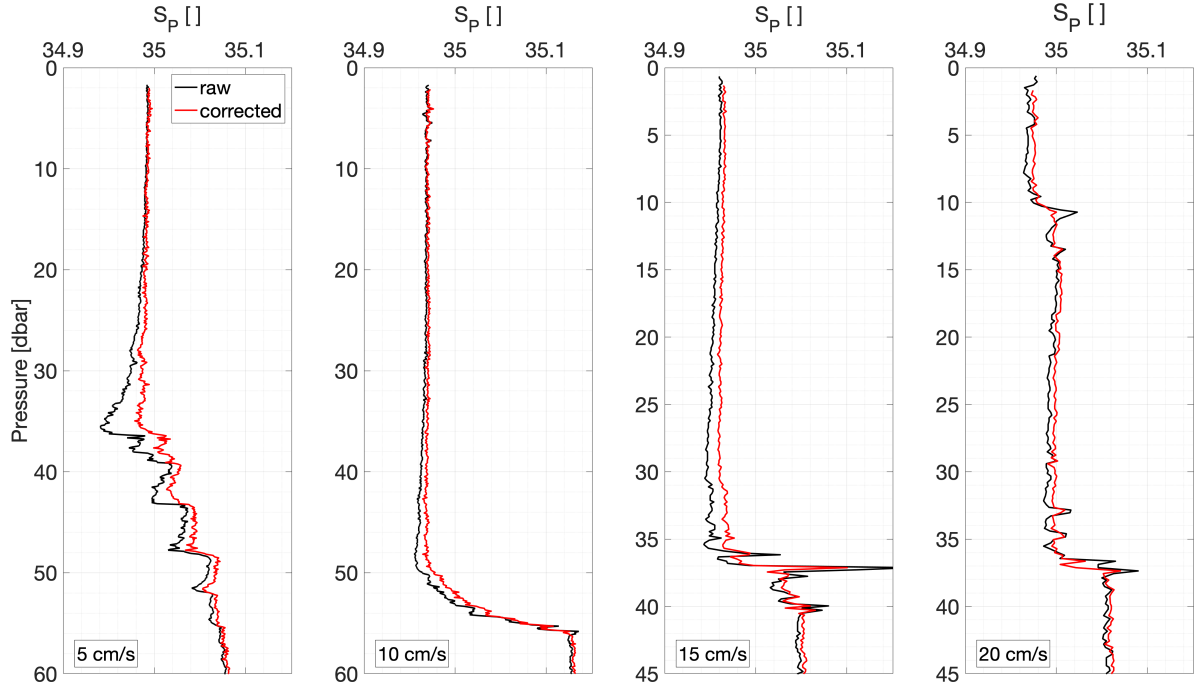
413 FIG. 11. Values of the measured ctcoeff , α , and τ as a function of the flume speed V_p (black circles).
 414 The standard deviation in the water speed measured during each plunge is shown as error bars. A power-law
 415 least-squares fit is applied to the data (dashed black line).

411 Morison et al. 1994). Figure 11 shows how each of the coefficients vary with the flow speed. All
 412 three coefficients can be fit to a power-law:

$$\begin{aligned} \text{ctcoeff} &= 0.07 \times V_p^{-0.86} + 7.5 \times 10^{-9} \\ \alpha &= 0.53 \times V_p^{-1.12} + 1.6 \times 10^{-7} \\ \tau &= 14.35 \times V_p^{-0.24} + 2.2 \times 10^{-5} \end{aligned}$$

416 which, for the nominal speed of Argo floats of 10 cm/s, yields $\text{ctcoeff} = 0.97 \times 10^{-2}$, $\alpha = 0.041$, and
 417 $\tau = 8.11$ s.

418 The validity of the thermal inertia correction across a range of profiling speeds is assessed using
 419 an Argo float profiling in the sub-Arctic North Atlantic. The float was set to profile at different
 420 speeds, ranging from 3 cm/s to 20 cm/s. Figure 12 shows the effect of the dynamic correction
 421 algorithm at four different speeds. While the amplitude of the correction is relatively small, due
 422 to the small temperature gradient, the corrected salinity does demonstrate reduced spiking at the
 423 interface (particularly visible at higher speeds), and a more homogeneous mixed layer over both
 424 shorter and longer timescales.



425 FIG. 12. Profile of practical salinity collected by float WMO4903275 at different profiling speeds as the float
 426 crosses a 1.5 to 2 °C temperature gradient. Raw data are shown in black, while data corrected for dynamic errors
 427 are shown in red.

428 5. Discussion

429 The accuracy of both temperature and pressure on the RBRargo³ CTD is proven to be within the
 430 expected accuracy of the Argo program (± 0.002 °C and ± 2.4 dbar, respectively; Wong et al. 2020),
 431 throughout the range of typical pressure experienced by a Core Argo floats (i.e., 2,000 dbar).

432 While salinity is calibrated at the factory to be within the Argo accuracy requirements at atmo-
 433 spheric pressure (± 0.01), a salinity error is introduced as pressure increases due to the physical
 434 deformation of the conductivity cell. This salinity bias is known to affect both inductive and
 435 electrode-based CTDs: while a salty bias is observed at depth in the RBRargo³, the electrode-
 436 based SBE41CP reports a fresh bias at depth (Sea-Bird Electronic, Inc. 2013). A unit-based
 437 compressibility correction to conductivity is determined using a laboratory setup where each
 438 RBRargo³ is pressurized in saltwater and a cubic correction to conductivity is derived (Figure
 439 5). The proposed correction is validated in the field and is proven to reduce the salinity bias with
 440 pressure (Figure 4).

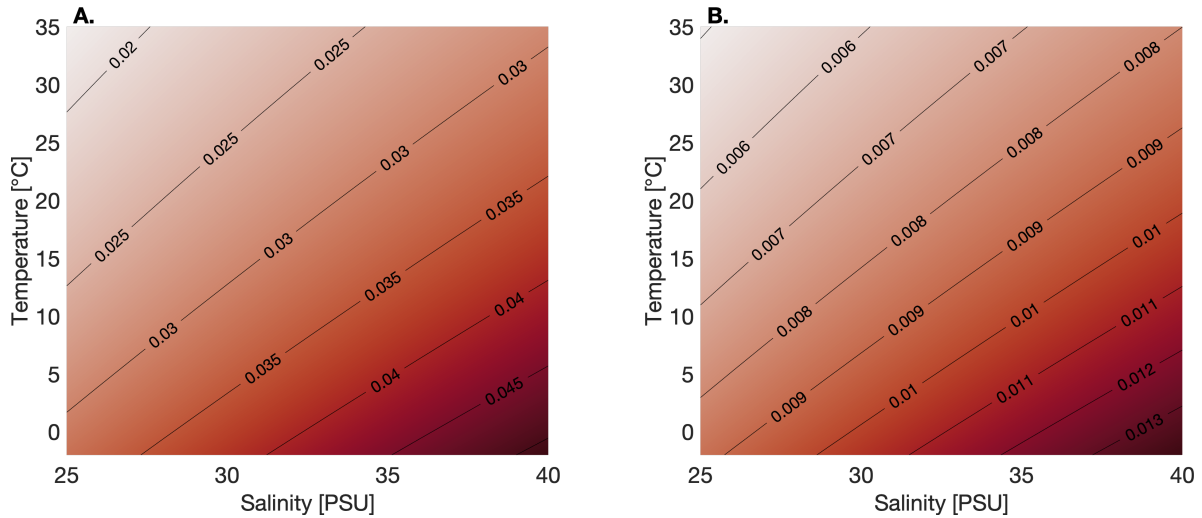
441 Of the nineteen RBRargo³ CTDs deployed for longer than 6 months, only one was found to
442 drift, which has been linked to a float malfunction leading to an excessive surface time likely
443 enabling significant biofouling to occur (Figure 6; RBR Report 2021). Despite the relatively short
444 time series available (average of 1.5 year), the RBRargo³ CTD presents an encouraging long-term
445 salinity stability with 94% (99.8%) of profiles within ± 0.01 (0.02) of the reference dataset.

446 For a profiling platform such as Argo floats, dynamic errors can significantly affect the quality
447 of the data. These errors are generated by profiling through vertical temperature gradients in the
448 water column. The most documented dynamic error, referred to as the C-T lag, is the result of
449 a difference in the inherent time-response of the thermistor with respect to the conductivity cell,
450 as well as any physical distance between the location of the two sensors (Horne and Toole 1980;
451 Lueck and Picklo 1990). A robust statistical analysis based on existing literature (Barth et al.
452 1996; Dever et al. 2020) determines that an optimal lag of 0.35 s helps minimize salinity spiking
453 for the RBRargo³ CTD. The absence of fall-rate dependence on the C-T lag demonstrates that the
454 thermistor and conductivity cell are relatively well-aligned in space, thus minimizing the advective
455 component of the C-T lag (Figure 7). The value determined here compares well with previous
456 estimate obtained in Halverson et al. (2020a) using a different method. This empirically estimated
457 C-T lag also agrees with the theoretical value. The response time stated by the manufacturer of
458 the thermistor used on the RBRargo³ CTD is around 0.70 s. If the conductivity measurement is
459 assumed to be instantaneous, then a lag of 0.35 s would be expected to best align the temperature
460 to the conductivity and minimize salinity spiking. Some minimal spiking would remain, however,
461 due to the fact that the temperature signal would be smoother than the conductivity readings, as it is
462 clearly observed in Figure 8. This remaining error can be mitigated by smoothing the conductivity
463 signal, or by applying a sharpening algorithm to the temperature, as suggested in Halverson et al.
464 (2020a). Inferring an unresolved high-frequency signal is a highly subjective task and is thus
465 left to the discretion of the data user. The uncertainty in the optimal C-T lag obtained from the
466 distribution in Figure 7 inevitably leads to an uncertainty in the corrected salinity. The magnitude
467 of the propagated error is directly proportional to the temperature gradient and the ascent rate.
468 As an example, a temperature gradient of 1°C/m sampled at an ascent rate of 10 cm/s leads to a
469 gradient of 0.1°C/s. The standard deviation in the determined optimal C-T lag ($\sigma=0.003$ s) thus
470 generates an error of about 3×10^{-4} °C, leading to an error in salinity of approximatively 3×10^{-4} .

471 Thermal inertia errors affecting salinity from the RBR $argo^3$ CTD exhibit two separate timescales.
472 The long-term thermal inertia error has a timescale $\mathcal{O}(120$ s), and generates an error on salinity
473 about four times smaller than its short-term counterpart (Figure 13). The correction for this second-
474 order thermal inertia error is based on the direct measurement of the instantaneous temperature
475 difference between the inside of the conductivity cell and the marine temperature. Implementing
476 the correction as a function of the temperature difference presents key advantages: First, it does not
477 require an explicit timescale, as the timescale is implicitly included in the temperature gradient.
478 Second, it prevents the propagation of spurious measurement anomalies throughout the time
479 series, as a recursive filter like L&P90 would. And third, being an instantaneous correction, it has
480 significant operational advantages as implementing the correction on board autonomous platforms
481 such as Argo floats is greatly simplified. Just like the C-T lag, the uncertainty associated with the
482 parameter ctcoeff that propagates onto the computed salinity can be estimated by considering once
483 more a temperature gradient of $0.1^\circ\text{C}/\text{s}$ sampled at 10 cm/s . The propagated uncertainty on the
484 salinity correction from the long-term thermal inertia correction is $<1\times10^{-3}$.

485 A short-term error is observed on a timescale of 5 to 10 s, and is corrected for using the L&P90
486 recursive model. As suggested in Morison et al. (1994), the correction is applied by inferring the
487 temperature of the sampled volume based on the marine temperature history (see Equation 4). The
488 amplitude of the correction on the salinity is thus both temperature and salinity dependent, and
489 is dictated by the a parameter in Equation 5 (see Figure 13). The uncertainty of the correction
490 using the L&P90 model is difficult to estimate, as it first requires estimating a timescale of the
491 adjustment (i.e., τ), and a corresponding amplitude (α). Additionally, these two parameters have
492 been observed to be inter-dependent (Morison et al. 1994; Lueck and Picklo 1990; Martini et al.
493 2019), suggesting than the uncertainty associated with the inferred timescale also affects the
494 amplitude of the correction. Finally, the L&P90 model being a recursive filter, the error in the
495 correction associated with the model's parameters uncertainty accumulates through time.

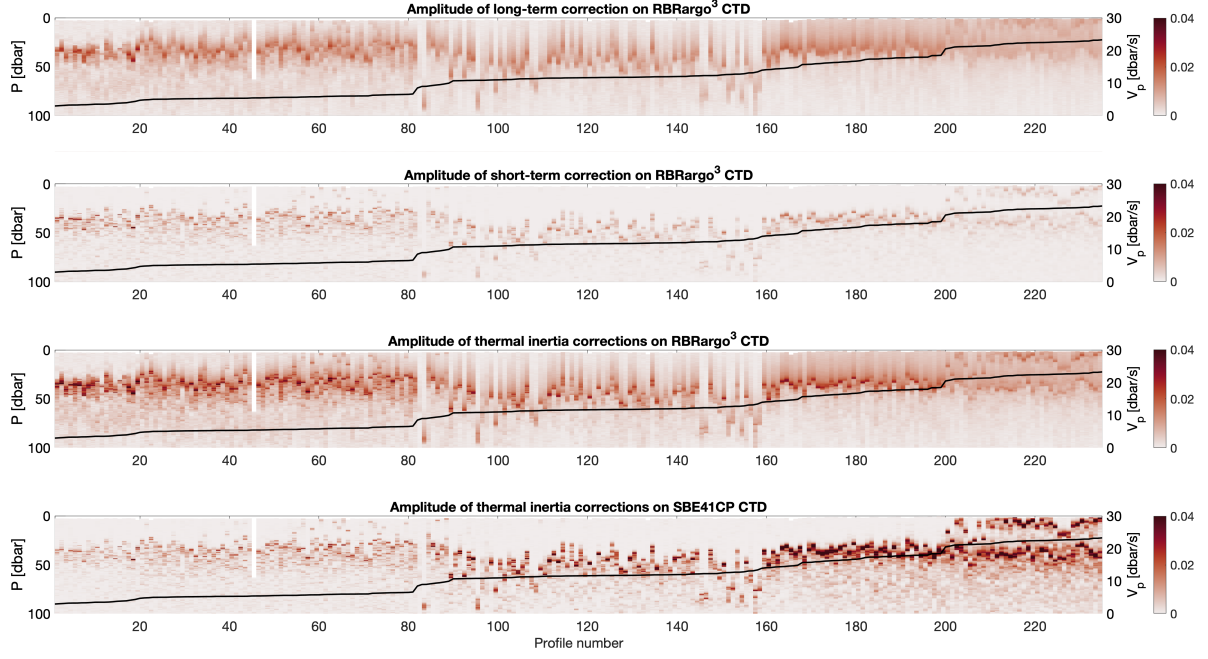
496 For comparison, the amplitude of the short-term thermal inertia correction on the RBR $argo^3$ is
497 about three times smaller than the corrections currently applied to CTD data collected from an
498 SBE41CP, and operates over similar timescales (Johnson et al. 2007). While the long-term thermal
499 inertia correction on the RBR $argo^3$ has a comparable amplitude to the short-term correction, its
500 longer timescales implies that the error is smeared over a larger part of the profiles. In particular,
501



496 FIG. 13. Amplitude of the salinity error (in 1°C) corrected by (A.) the short-term
 497 thermal inertia corrections, as a function of the measured temperature and salinity.

503 profiles collected in tropical waters would be more affected by thermal inertia errors due to the
 504 temperature gradients in these regions, often characterized by deeper and sharper temperature
 505 gradients. The total amplitude of thermal inertia corrections on the RBRargo³ is highly dependent
 506 on the vertical temperature structure of the water column and is therefore difficult to characterize
 507 theoretically. An example of the amplitude of each thermal inertia correction is shown in Figure
 508 14 using the high-resolution data returned by the float for a short period of time (See Table 5).
 509 As expected, the maximum amplitude of the thermal inertia correction on a RBRargo³ is weaker
 510 than on the SBE41CP, but the correction affects a larger portion of the water column, due to the
 511 long-term component of the thermal inertia.

517 Because thermal inertia errors are generated from the heat exchange between the conductivity cell
 518 and its surrounding water, the thermal inertia corrections derived in this study are expected to be a
 519 function of the profiling speed. The range of speeds explored in the flume not only encompasses
 520 the nominal speed for Argo floats ($\sim 10 \text{ cm/s}$), but also covers the realistic range of speeds an
 521 autonomous profiling platform can achieve (e.g., floats, gliders). The relationship linking the three
 522 coefficients to profiling speed are modelled using a power-law, as the theoretical work from Lueck
 523 (1990) suggests, but it is not intended to be anything more than an empirical fit. Caution should
 524 be used when extrapolating coefficients outside of the range of explored speeds, such as for typical
 525 CTD rosette profiling speeds (e.g., 100 cm/s).



512 FIG. 14. Amplitude of the salinity correction for thermal inertia determined from high-resolution profiles
 513 collected by WMO4903275 at the base of the mixed layer.(first row) long-term correction on an RBRargo³ ,
 514 (second row) short-term correction on an RBRargo³, (third row) total thermal inertia correction on an RBRargo³,
 515 and (fourth row) total thermal inertia correction for a SBE41CP (Johnson et al. 2007). Profiles are organized by
 516 increasing profiling speed V_p .

526 One of the most important results of the dependence on flow-rate is the fact that, due to the
 527 shape of the power-law function, the three coefficients are not only weaker, but they are also less
 528 dependent on the profiling speed (Figure 11). The main consequence is that the thermal inertia
 529 correction is thus less sensitive to uncertainties in both coefficients and flow-rates when profiling
 530 at higher speeds. To minimize the uncertainty on the thermal inertia correction, it is therefore
 531 recommended to profile at higher speeds, which could be compensated with a higher sampling
 532 rate to preserve vertical resolution. This can be directly observed in Figures 12 and 14, where the
 533 salinity error visible in the raw in-situ data is clearly smaller at faster speeds, despite crossing a
 534 similar temperature gradient (1.5 to 2°C).

535 For an RBRargo³ profiling at approximatively 10 cm/s the best practices for dynamic correc-
 536 tioncan be summarized as: (1) lagging the temperature signal by -0.35 s, (2) correcting for the

537 long-term thermal inertia error using Equation 3 and $\text{ctcoeff} = 9.7 \times 10^{-3}$, and (3) correcting for the
538 short-term thermal inertia error using L&P90 (Equations 4 and 5) with $\alpha = 0.041$ and $\tau = 8.11\text{s}$.

539 *Acknowledgments.* Drs. Owens and Richards contributed to the characterization of the thermal
 540 inertia errors. Dr. Wijffels lead the validation of pressure and temperature measurements on a
 541 RBRargo³. Dr. Wong conducted the analysis of salinity measurement stability. Drs. Shkvorets,
 542 Halverson, and Johnson provided support in the experimental design and analysis of the compress-
 543 ibility error in salinity. Thanks go to the Argo community at large, for their support in facilitating
 544 deployments of RBRargo³ CTDs, in providing ancillary datasets, and in offering feedback on the
 545 analysis. Special thanks are directed to the “Argo RBR Data Task Team”, specially formed to
 546 collaborate on the analysis of the RBRargo³.

547 *Data availability statement.* The data used in this work is available in a dedicated GitHub repos-
 548 itory: https://github.com/matdever/RBRargo3_paper. The code necessary to produce the
 549 displayed figures are also included in the repository.

550

APPENDIX A

551

Datasets

TABLE A1. List of the datasets obtained from field cruises used to characterize the RBRargo³.

Cruise name	Partner Institution	Year	Ocean basin	RBRargo ³ S/Ns
Line P	DFO Canada	2018	Northeast Pacific Ocean	060672
JAMSTEC	JAMSTEC	2018	Northwest Pacific Ocean	060669, 060671
PEACH	WHOI	2018	Northwestern Atlantic Ocean	060667, 060668, 060671
AR41	WHOI	2019	Northwestern Atlantic Ocean	060667, 060668, 060670
YMC	CSIRO/WHOI	2019	Southeastern Indian Ocean	060669, 060671

DFO = Department of Fisheries and Ocean

JAMSTEC = Japan Agency for Marine-Earth Science and Technology

WHOI = Woods Hole Oceanographic Institution

CSIRO = Commonwealth Scientific and Industrial Research Organisation.

TABLE A2. List of the datasets obtained from profiling floats used to characterize the RBRargo³.

Float type	Float ID	Data resolution	Institution	Year	Ocean basin
ALAMO	9139	1 Hz	WHOI	2017	Caribbean Sea
Argo float	WMO4903275	0.10 dbar bins	WHOI	2020	North Atlantic

WHOI = Woods Hole Oceanographic Institution

552

APPENDIX B

553

Calibration of rosette data

554 Similar to SBE911 cross-calibration protocol, bottle salinity samples collected from the CTD
555 rosette can be used to cross-calibrate RBRargo³ CTDs mounted on a shipboard rosette. Inductive
556 conductivity cells, like the one on the RBRargo³, are subject to the proximity effect: Any material
557 located within a 15 cm radius from the conductivity cell would affect measurements of conductivity
558 in a multiplicative way (Halverson et al. 2020b). The multiplicative factor is named the K-factor:

$$C = K \times C_{raw} \quad (\text{B1})$$

559 A conductive material, such as a metal, would generate a K-factor smaller than 1 (i.e., the
560 apparent conductivity would appear larger than the one of the water), while an insulating material
561 such as plastic would lead to a K-factor greater than 1 (i.e., the apparent conductivity would appear
562 smaller than the one of the water). The two RBRargo³ CTDs mounted on the rosette during the
563 YMC cruise onboard the RV Investigator in 2019 (serial numbers 060669 and 060671; Rees, C. and
564 McMahon, M. 2019) are cross-calibrated with salinity water samples measured using an AutoSal
565 Guildline using a zero-intercept linear fit (see Equation B1). A K-factor of 1.0001 and 0.9997 are
566 obtained for SN060669 and SN060671, respectively.

567 References

- 568 Barth, J. A., R. O'Malley, J. Fleischbein, R. L. Smith, and A. Huyer, 1996: Seasoor and ctd
569 observations during the coastal jet separation cruise w9408a, august to september 1994. Tech.
570 Rep. 162, College of Oceanic and Atmospheric Sciences, Oregon State University, 170 pp pp.
- 571 Bittig, H. C., B. Fiedler, R. Scholz, G. Krahmann, and A. Kötzinger, 2014: Time response
572 of oxygen optodes on profiling platforms and its dependence on flow speed and temperature.
573 *Limnology and Oceanography: Methods*, **12** (8), 617–636, <https://doi.org/10.4319/lom.2014.12.617>.
- 575 Cabanes, C., V. Thierry, and C. Lagadec, 2016: Improvement of bias detection in argo float conduc-
576 tivity sensors and its application in the north atlantic. *Deep Sea Research Part I: Oceanographic*
577 *Research Papers*, **114**, 128–136, <https://doi.org/10.1016/j.dsr.2016.05.007>.
- 578 Dever, M., M. Freilich, J. T. Farrar, B. Hodges, T. Lanagan, A. J. Baron, and A. Mahadevan,
579 2020: EcoCTD for Profiling Oceanic Physical–Biological Properties from an Underway Ship.

- 580 *Journal of Atmospheric and Oceanic Technology*, **37** (5), 825–840, <https://doi.org/10.1175/JTECH-D-19-0145.1>.
- 582 Fozdar, F. M., G. J. Parkar, and J. Imberger, 1985: Matching temperature and conductivity
583 sensor response characteristics. *Journal of Physical Oceanography*, **15** (11), 1557 – 1569,
584 [https://doi.org/10.1175/1520-0485\(1985\)015<1557:MTACSR>2.0.CO;2](https://doi.org/10.1175/1520-0485(1985)015<1557:MTACSR>2.0.CO;2).
- 585 Halverson, M., I. Shkvorets, and G. Johnson, 2020a: Dynamic corrections for the RBRargo CTD
586 2000dbar. Tech. rep., RBR, 1–26 pp. URL <https://oem.rbr-global.com/floats/files/5898249/34668603/1/1586804683000/0008228revA+Dynamic+corrections+for+the+RBRargo+CTD+2000dbar.pdf>.
- 589 Halverson, M., E. Siegel, and G. Johnson, 2020b: Inductive-conductivity cell a primer on high
590 accuracy ctd technology. *Sea Technology*, **61** (2), 24–27.
- 591 Horne, E. P. W., and J. M. Toole, 1980: Sensor Response Mismatches and Lag Correction
592 Techniques for Temperature-Salinity Profilers. *Journal of Physical Oceanography*, **10** (7), 1122–
593 1130, [https://doi.org/10.1175/1520-0485\(1980\)010<1122:SRMALC>2.0.CO;2](https://doi.org/10.1175/1520-0485(1980)010<1122:SRMALC>2.0.CO;2).
- 594 Jayne, S. R., and N. M. Bogue, 2017: Air-deployable profiling floats. *Oceanography*,
595 <https://doi.org/10.5670/oceanog.2017.214>.
- 596 Johnson, G. C., 2020: Comments on “Corrections for Pumped SBE 41CP CTDs Determined
597 from Stratified Tank Experiments”. *Journal of Atmospheric and Oceanic Technology*, **37** (2),
598 351–355, <https://doi.org/10.1175/JTECH-D-19-0098.1>.
- 599 Johnson, G. C., J. M. Toole, and N. G. Larson, 2007: Sensor Corrections for Sea-Bird SBE-
600 41CP and SBE-41 CTDs. *Journal of Atmospheric and Oceanic Technology*, **24** (6), 1117–1130,
601 <https://doi.org/10.1175/JTECH2016.1>.
- 602 Lueck, R. G., 1990: Thermal Inertia of Conductivity Cells: Theory. *Journal of Atmospheric
603 and Oceanic Technology*, **7** (5), 741–755, [https://doi.org/10.1175/1520-0426\(1990\)007<0741:TIOCCT>2.0.CO;2](https://doi.org/10.1175/1520-0426(1990)007<0741:TIOCCT>2.0.CO;2).
- 604 Lueck, R. G., and J. J. Picklo, 1990: Thermal Inertia of Conductivity Cells: Observations with a
605 Sea-Bird Cell. *Journal of Atmospheric and Oceanic Technology*, **7** (5), 756–768, [https://doi.org/10.1175/1520-0426\(1990\)007<0756:TIOCCO>2.0.CO;2](https://doi.org/10.1175/1520-0426(1990)007<0756:TIOCCO>2.0.CO;2).

- 608 Martini, K. I., D. J. Murphy, R. W. Schmitt, and N. G. Larson, 2019: Corrections for Pumped
609 SBE 41CP CTDs Determined from Stratified Tank Experiments. *Journal of Atmospheric and*
610 *Oceanic Technology*, **36** (4), 733–744, <https://doi.org/10.1175/JTECH-D-18-0050.1>.
- 611 Morison, J., R. Andersen, N. Larson, E. D'Asaro, and T. Boyd, 1994: The Correction for Thermal-
612 Lag Effects in Sea-Bird CTD Data. *Journal of Atmospheric and Oceanic Technology*, **11** (4),
613 1151–1164, [https://doi.org/10.1175/1520-0426\(1994\)011<1151:TCFTLE>2.0.CO;2](https://doi.org/10.1175/1520-0426(1994)011<1151:TCFTLE>2.0.CO;2).
- 614 Nezlin, N. P., and Coauthors, 2020: Accuracy and long-term stability assessment of inductive
615 conductivity cell measurements on argo floats. *Journal of Atmospheric and Oceanic Technology*,
616 **37** (12), 2209 – 2223, <https://doi.org/10.1175/JTECH-D-20-0058.1>.
- 617 Owens, W. B., and A. P. Wong, 2009: An improved calibration method for the drift of the
618 conductivity sensor on autonomous ctd profiling floats by θ -s climatology. *Deep Sea Research*
619 *Part I: Oceanographic Research Papers*, **56** (3), 450–457, [https://doi.org/10.1016/j.dsr.2008.09.](https://doi.org/10.1016/j.dsr.2008.09.008)
620 008.
- 621 RBR Report, 2021: Argo float WMO5906299: Analysis of fresh salinity anomalies. Tech.
622 rep., RBR. URL https://oem.rbr-global.com/floats/files/5898249/46235845/1/1624471832000/0011136revA+Argo+float+WMO5906299_+Analysis+of+fresh+salinity+anomalies.pdf.
- 624 Rees, C. and McMahon, M., 2019: Rv investigator hydrochemistry data processing report. Tech.
625 rep., CSIRO.
- 626 Roemmich, D., and Coauthors, 2019: On the Future of Argo: A Global, Full-Depth, Multi-
627 Disciplinary Array. *Frontiers in Marine Science*, **6**, <https://doi.org/10.3389/fmars.2019.00439>.
- 628 Sanabia, E. R., and S. R. Jayne, 2020: Ocean observations under two major hurricanes: Evolution
629 of the response across the storm wakes. *AGU Advances*, **1** (3), e2019AV000161, <https://doi.org/10.1029/2019AV000161>.
- 631 Schmitt, R. W., R. C. Millard, J. M. Toole, and W. D. Wellwood, 2005: A double-diffusive
632 interface tank for dynamic-response studies. *Journal of Marine Research*, **63** (1), 263–289,
633 <https://doi.org/10.1357/0022240053693842>.

- 634 Sea-Bird Electronic, Inc., 2013: Compressibility compensations of sea-bird conductivity sensors.
635 Tech. Rep. Application note No. 10, Sea-Bird Electronic, Inc. URL [http://www.seabird.com/
636 application-notes](http://www.seabird.com/application-notes).
- 637 Ullman, D. S., and D. Hebert, 2014: Processing of Underway CTD Data. *Journal of Atmospheric
638 and Oceanic Technology*, **31** (4), 984–998, <https://doi.org/10.1175/JTECH-D-13-00200.1>.
- 639 Wong, A. P. S., G. C. Johnson, and W. B. Owens, 2003: Delayed-mode calibration of autonomous
640 ctd profiling float salinity data by θ -s climatology. *Journal of Atmospheric and Oceanic Tech-
641 nology*, **20** (2), 308 – 318, [https://doi.org/10.1175/1520-0426\(2003\)020<0308:DMCOAC>2.0.
643 dmcoac_2_0_co_2.xml](https://doi.org/10.1175/1520-0426(2003)020<0308:DMCOAC>2.0.
642 CO;2).
- 644 Wong, A. P. S., and Coauthors, 2020: Argo data 1999–2019: Two million temperature-salinity
645 profiles and subsurface velocity observations from a global array of profiling floats. *Frontiers in
646 Marine Science*, **7**, 700, <https://doi.org/10.3389/fmars.2020.00700>.